ADVANCED FUNCTIONAL MATERIALS
www.afm-journal.de

Storable Polydopamine Nanoparticles Combined with Bacillus Calmette-Guérin for Photothermal-Immunotherapy of Colorectal Cancer

Ze-Nan Zhuang, Yong-Dan Qi, Qian-Xiao Huang, Cheng Zhang, Xuan Zeng, Zhen-Lin Zhong,* Si-Xue Cheng, and Xian-Zheng Zhang**

Photothermal immunotherapy emerges as a promising strategy for treating tumors. However, the majority of current photothermal immunotherapy approaches do not yet show significant potential for clinical translation. In this study, lyophilized polydopamine (PDA) nanoparticles combined with Bacillus Calmette–Guérin (BCG) are investigated for photothermal immunotherapy against colorectal cancer. By simply mixing with two lyophilized powders, PDA nanoparticles can covalently bond onto BCG to form BCG@PDA. This combination demonstrates a potent photothermal cytotoxic effect on tumor cells by utilizing PDA nanoparticles. In addition, a heightened immune response triggered by the BCG vaccine, as evidenced by the secretion of important pro-inflammatory cytokines and the activation of antigen-presenting cells, is observed. In vivo testing on a murine colon cancer model demonstrates that the combined treatment significantly inhibits tumor growth. Further, the lyophilized PDA nanoparticles can be stored at −20 °C for up to 1 year with stable photothermal properties. Therefore, this study not only presents a reliable method for storing the therapeutic PDA nanoparticles but also demonstrates the potential application of BCG@PDA in photothermal immunotherapy for colorectal cancer.

1. Introduction

Colorectal cancer (CRC), the most common type of gastrointestinal tumor, is the second cause of cancer deaths and has a high incidence worldwide.[1] Surgery combined with chemotherapy is the standard treatment for stage II–III CRC patients.[2] However, the restriction of tumor tissues, especially the rectum, could bring serious damage to the life qualities of patients. It is an urgent question to develop new therapies directed at CRC.

Photothermal therapy (PTT), a minimally invasive cancer treatment that causes localized thermal damage under irradiation by near-infrared (NIR), has attracted extensive interest over the past few decades. The focus of most preclinical PTT studies is photothermal contrast agents, such as polydopamine (PDA),[3] gold nanomaterials,[4] indocyanine green,[5] and black phosphorus.[6] These photothermal agents extend excellent photothermal conversion capacity and negligible toxicity. However, phototherapy (including PTT and photodynamic therapy) requires some extreme conditions, such as high-energy laser light and precise localization, which limit phototherapy to many certain dermatological indications in clinical.[7] A lot of research focuses on the development of light delivery paradigms such as interstitial irradiation and interventional photodynamic therapy.[8] Considering the specific position of the colorectum, the employment of interventional phototherapy in gastrointestinal tumors could have a promising future. In the meantime, PTT can induce immunogenic cell death (ICD) of tumor cells, which releases tumor antigens to induce local immunoreaction.[9] However, the therapeutic outcome is still unsatisfactory due to the weak immune signal that is solely attributed to PTT.[10] Hence, it is essential to devise a combined therapeutic strategy to enhance the treatment efficacy of PTT.

As Coley et al. coincidentally observed tumor regression in a patient with bacterial infection, the use of microorganisms for cancer immunotherapy has garnered more attention in the last few years, such as bacteria,[11] microalgae,[12] and viruses.[13] However, the progress of utilizing live bacteria for therapeutic purposes in clinical settings is significantly impeded by the potential risks of infection-related toxicities. An instance of success can be seen in the case of Bacillus Calmette–Guérin (BCG), which consists of live *Mycobacterium tuberculosis* and is utilized in the clinical setting for the management of bladder cancer.[14]

Z.-N. Zhuang, Y.-D. Qi, Q.-X. Huang, C. Zhang, X. Zeng, Z.-L. Zhong, S.-X. Cheng, X.-Z. Zhang
Key Laboratory of Biomedical Polymers of Ministry of Education and Department of Chemistry
Wuhan University
Wuhan 430072, P. R. China
E-mail: xz-zhang@whu.edu.cn; zlzhong@whu.edu.cn; xuanzeng@whu.edu.cn
X.-Z. Zhang
Cancer Precision Diagnosis and Treatment and Translational Medicine Hubei Engineering Research Center
Zhongnan Hospital of Wuhan University
Wuhan 430071, P. R. China

The ORCID identification number(s) for the author(s) of this article can be found under https://doi.org/10.1002/adfm.202404381

DOI: 10.1002/adfm.202404381

In clinical settings, BCG immunotherapy is the optimal adjuvant treatment for non-muscle-invasive bladder cancer with a high risk of progression. It is one of the best biotherapies for cancer being used; although, its mechanism is still under investigation.[15] Available evidence indicates that BCG could trigger a robust antitumoral nonspecific immune response.[14a] In addition, some clinical trials show that the BCG vaccine could improve the prognosis of patients with CRC.[16] With these advantages, we believe that BCG could play a more important role in CRC treatment.

In this paper, we proposed a novel CRC treatment strategy that used PDA nanoparticles as the photothermal contrast agent in combination with BCG vaccines to trigger a robust antitumor immune response. First, we synthesized PDA nanoparticles and acquired the storable user-friendly lyophilized PDA nanoparticle powder by using glucose as a stabilizer (**Figure 1A**). We found PDA nanoparticles could be stably stored at −20 °C for at least 1 year. We found lyophilized protectants might improve the stability of PDA preservation, which is very beneficial for its subsequent production, preservation, and transportation. Then, the lyophilized powder and BCG vaccines were mixed to form material-assisted microorganisms (BCG@PDA) for tumor treatment (Figure 1B). With the intratumoral injection, BCG@PDA provided an excellent photothermal killing effect. The thermal damage to tumor cells induced ICD to release tumor antigens, including adenosine triphosphate (ATP), calreticulin (CRT), and high mobility group protein B1 (HMGB1), which could activate the immune system and cause an inflammatory reaction. At the same time, BCG was capable of recruiting and activating macrophages at the tumor site. In particular, BCG modulated macrophages polarization to the M1 type, contributing to killing tumors and producing various antitumor cytokines (e.g., tumor necrosis factor-α [TNF-α] and interleukin-6 [IL-6]). Further, those tumor antigens and BCG vaccines also promoted dendritic cells (DCs) maturation and elicited an impressive antitumor T cell response (Figure 1C). In a word, we concentrated on the application of BCG in conjunction with photothermal-induced ICD to stimulate immunity in situ. This approach recruited a tumor-promoting enrichment of immune cells from the periphery of the tumor, thereby achieving a synergistic effect of combined immunotherapy and photothermal therapy.

2. Results

2.1. Synthesis and Characterization of PDA Nanoparticles

PDA nanoparticles were synthesized by a solution-oxidation method described previously.[3a] Scanning electron microscopy (SEM) imaging revealed that PDA nanoparticles were spherical and their average size was ≈220 nm (**Figure 2A**). Meanwhile, the hydrodynamic size of PDA nanoparticles was ≈240 nm with a negative charge on the surface (Figure 2B). High-performance liquid chromatography (HPLC) was used to monitor the concentration of dopamine during the preparation of PDA nanoparticles. After 24 h, the dopamine was consumed, which indicated the successful formation of PDA nanoparticles (Figure S1A, Supporting Information). We further examined the structure of PDA nanoparticles by Fourier transform infrared (FT-IR) spectrum. Compared with dopamine, the disappearance of $-NH_2$ characteristic peaks and the appearance of indole structures and C=O confirmed that we obtained PDA nanoparticles successfully (Figure S1B, Supporting Information). To achieve mass production of PDA nanoparticles, the dopamine hydrochloride feeding was increased to 5 g, and mechanical agitation was adopted (Figure 2C). The SEM imaging shows this method could be extended to gram-scale production of PDA nanoparticles with well-controlled morphology and size distribution (Figure 2D).

Then, the photothermal performance of PDA nanoparticles under the NIR (808 nm, 1 W cm^{-2}) was studied. As expected, the PDA nanoparticles exhibited excellent photothermal performance with the temperature rising by 27 °C in 5 min at a concentration of 100 μg mL^{-1} (Figure 2E; Figure S2, Supporting Information). Further, we explored the stabilities of PDA nanoparticles under different temperatures, pHs, and ultraviolet light irradiation. We found that PDA nanoparticles were stable under most conditions except ultraviolet light which promoted the aggravation of nanoparticles and precipitation (Figure S3, Supporting Information). The evidence indicated that we successfully obtained PDA nanoparticles with good stability.

2.2. Storage Stability of PDA Nanoparticles

Usually, nanoparticles are unstable in suspension, and lyophilization has been used to advance the long-term stabilities. Thus, we optimized the lyophilization of PDA nanoparticles by using different lyoprotectants.[17] As shown in Figure 2F, the PDA nanoparticles got a much smaller size when using sugars as lyoprotectants. Considering the smaller size distribution and the cost, glucose was chosen as the lyoprotectant of the PDA nanoparticles and obtained lyophilized PDA nanoparticles (Figure 2G). The SEM image also showed an average size of ≈220 nm, which was similar to untreated PDA nanoparticles (Figure 2F). In addition, when rehydrated, long-term storage lyophilized PDA nanoparticles under −20 °C exhibited a stable size, surface properties, and photothermal effects compared to storage under 4 °C (Figure 2H,I; Figure S4, Supporting Information). Obviously, the storable user-friendly lyophilized PDA nanoparticles we prepared had excellent redispersibility and stable size distribution.

Further, we investigated the feasibility of PDA nanoparticles as a PTT agent for tumor treatment by using the CT26 colon carcinoma cell line. Lyophilized PDA nanoparticles were incubated with CT26 cells for 4 h; and then, irradiated by 808 nm laser (1 W cm^{-2}) for 5 min. After that, the cell viability was evaluated by the MTT assay. In the PDA with laser group, almost 80% of cells were killed under the concentration of 50 μg mL^{-1} (Figure S5A, Supporting Information). Then, the cells were stained by calcein AM and propidium iodide (PI) (Figure S5B, Supporting Information). In addition, PDA nanoparticles exhibited negligible cytotoxicity in noncancerous 3T3 and NCM460 cells even at the concentration of 200 μg mL^{-1} (Figure S5C, Supporting Information). Subsequently, to investigate the photothermal conversion of PDA in vivo, CT26-bearing mice were intratumorally injected with PDA; and then, treated by an 808 nm laser

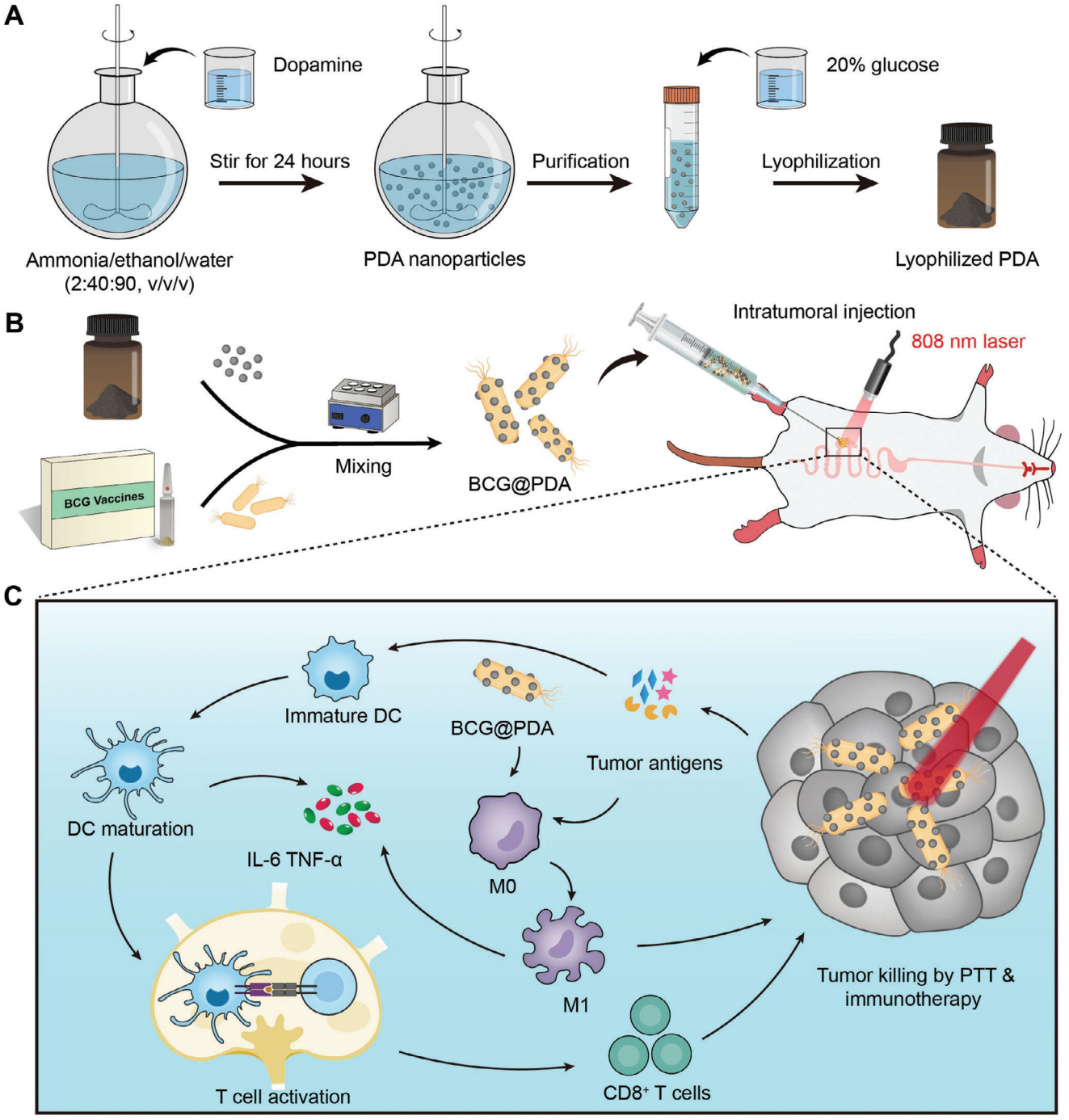

Figure 1. A schematic illustrating the preparation of BCG@PDA and its mechanism for potentiating photothermal cancer immunotherapy. A) Preparation of lyophilized PDA. B) Preparation of BCG@PDA and its usage for colorectal cancer. C) Photothermal tumor cell-killing effect of BCG@PDA and stimulation of innate immunity system induced by BCG@PDA.

(1 W cm^{-2}). As monitored by photothermography, the highest surface temperature was 46.6 °C in the PDA group; while, the PBS group had no obvious increase in temperature (Figure S6A,B, Supporting Information). These findings showed that storage PDA nanoparticles hold great potential as an efficient PTT agent for tumor therapy.

2.3. Combination of PDA Nanoparticles and Bacterium

Then, we used lyophilized powders of PDA nanoparticles and BCG vaccine to form BCG@PDA. First, two lyophilized powders were dispersed in phosphate buffer saline (PBS) to form suspensions, respectively. After that, two suspensions were mixed and oscillated for 30 min to obtain BCG@PDA (**Figure** 3A).

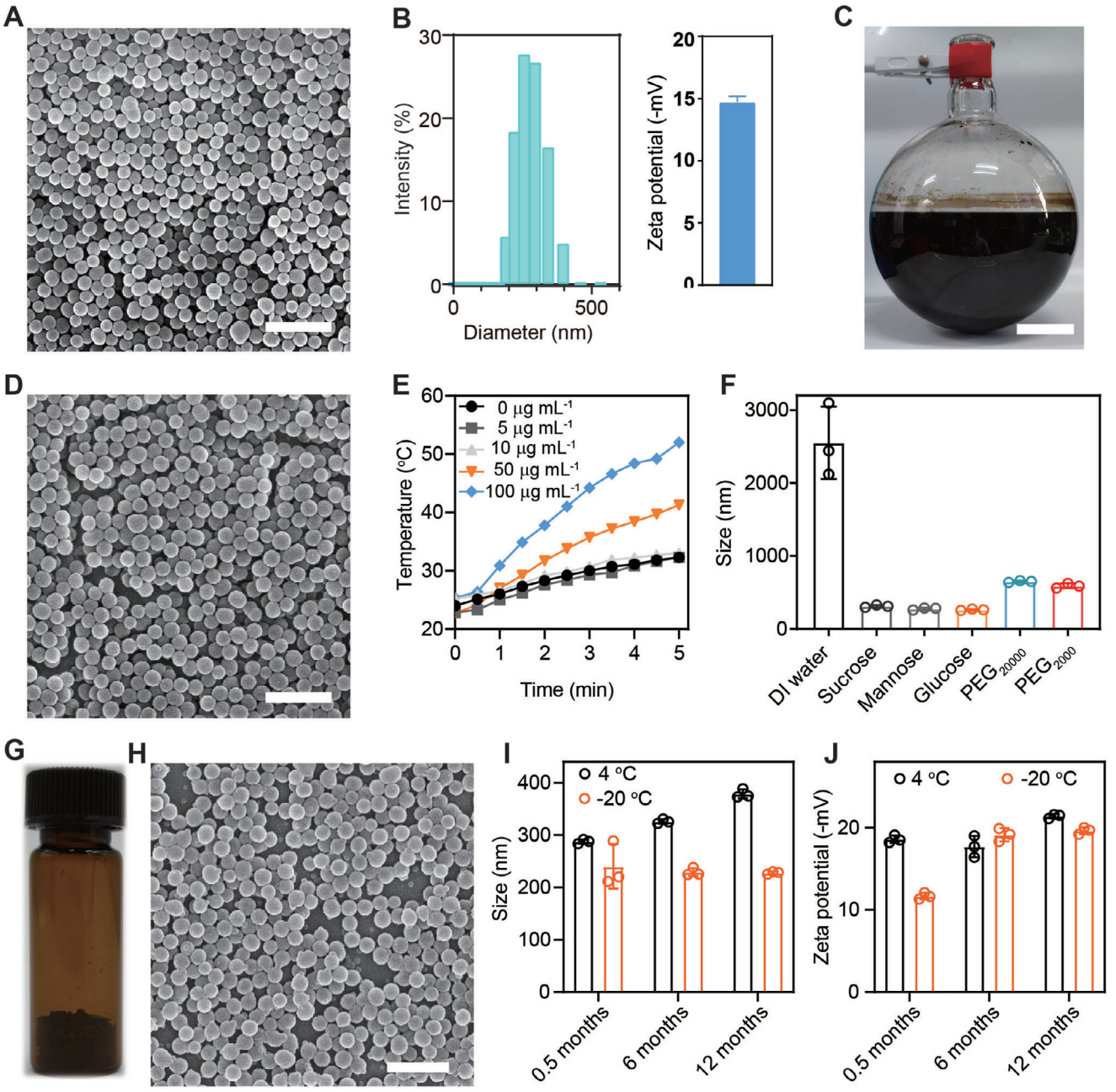

Figure 2. Preparation, characterization, and storage of PDA nanoparticles. A) SEM image of PDA nanoparticles (scale bar: 1 μm). B) Hydrodynamic size distribution and zeta potential of PDA nanoparticles. C) Photograph of PDA synthesis in 2 L round-bottom flask (scale bar: 5 cm). D) SEM image of PDA nanoparticles synthesized in 2 L round-bottom flask (scale bar: 1 μm). E) Photothermal profiles of PDA nanoparticles at different concentrations under 808 nm irradiation for 5 min. F) The hydrodynamic size of PDA nanoparticles after adding various lyoprotectants ($n = 3$). G) Photograph of lyophilized PDA nanoparticles stored in the brown bottle. H) SEM image of PDA nanoparticles after lyophilization, protected by glucose (scale bar: 1 μm). I,J) Hydrodynamic size distribution (I) and zeta potential (J) of PDA nanoparticles after storage for 0.5, 6, and 12 months ($n = 3$).

As we could see in SEM images, the PDA nanoparticles were closely combined with BCG (Figure 3B). To explore the adhesiveness of PDA nanoparticles, X-ray photoelectron spectroscopy (XPS) was used to determine the surface structure. The surface of PDA nanoparticles consisted of carbon, oxygen, and nitrogen elements (Figure 3C). The 1s peak of carbon (C 1s) of PDA contained four types of carbon bonds: C═C peak at 284.5 eV, C—C peak at 285.1 eV, C—OH and C—N peak at 286.1 eV, and C═O peak at 288.9 eV, respectively (Figure 3D). In addition, the two main peaks of O 1s represented the C—O bond at 533.8 eV and the C═O bond at 532.5 eV (Figure 3E). According to the fitting results, the ratio of C—O/C═O was determined based on the peak area analysis, yielding a proportion of 1.90 to 1. FT-IR characterization also confirmed the existence of O—H, C═O, and C—O

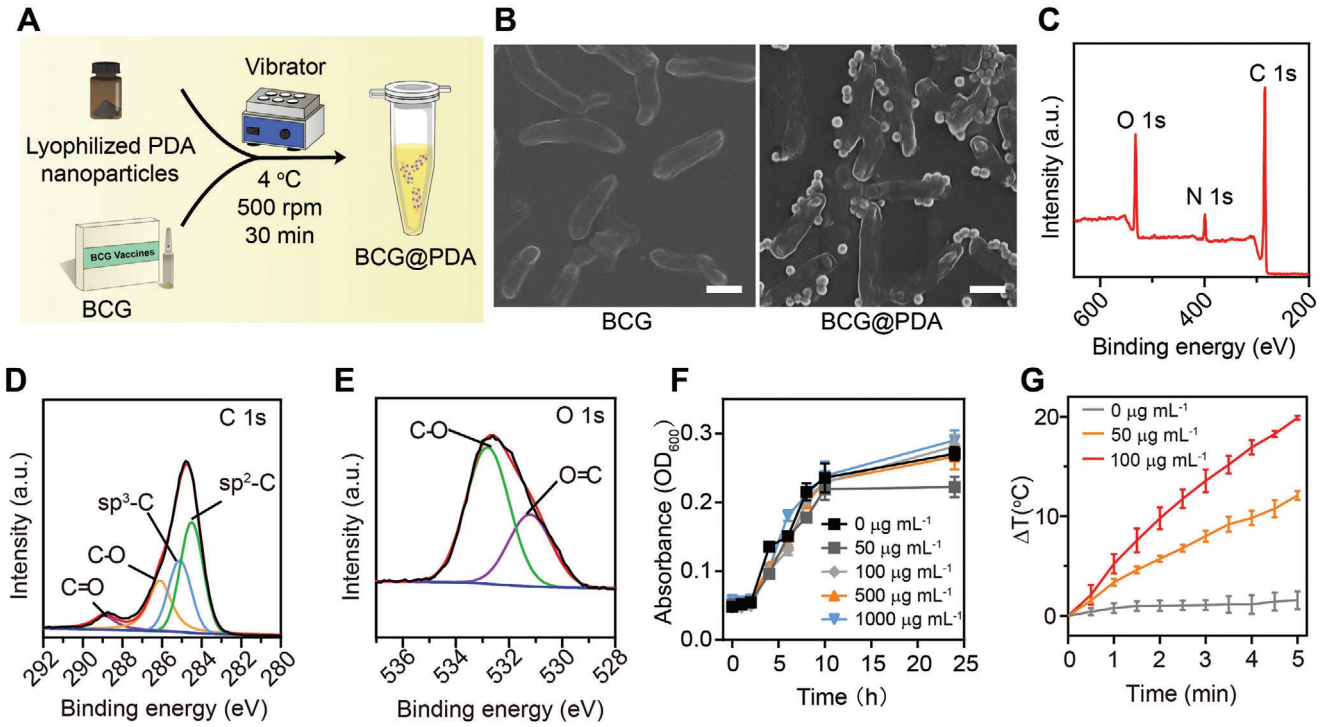

Figure 3. Preparation and characterization of BCG@PDA and Bac@PDA. A) Schematic illustrations of BCG@PDA preparation. B) SEM images of BCG and BCG@PDA (scale bar: 1 μm). C) XPS spectra of PDA. D) C 1s peaks. E) O 1s peaks. F) The OD_{600} of *E. coli* after combining with PDA at different concentrations (0, 50, 100, 500, and 1000 μg mL^{-1}) for 24 h ($n = 3$). G) Photothermal profiles of Bac@PDA under 808 nm (1 W cm^{-2}) irradiation for 5 min ($n = 3$) (Bac: 6×10^7 CFU mL^{-1}; PDA concentrations: 0, 50, and 100 μg mL^{-1}).

bonds (Figure S1B, Supporting Information). Based on this evidence, we predicted that the surface of PDA might be a structure of catechol and o-quinone which could react with bacterial amine and thiol groups by Michael-type addition and Schiff base reactions. Thus, we could successfully obtain the PDA nanoparticle-modified BCG by mixing two redispersed lyophilized powders easily.

To investigate the applicability and advantage of our combined strategy, *Escherichia coli* MG1655 was employed as a model organism to investigate the effects of PDA modification. First, the combination of bacteria and PDA nanoparticles was studied. We found that bacteria were able to combine above 77% of PDA nanoparticles even when the concentration of PDA rose to 500 μg mL^{-1} (Figure S7A–C, Supporting Information). Then, the bacterial activity after binding with PDA nanoparticles was examined at different concentrations. We found that PDA nanoparticles had negligible influence on bacterial proliferation even at a concentration of 1 mg mL^{-1} (Figure 3F). Then, a chemotaxis assay was prepared to study the mobilities of bacteria. The mCherry-labeled *E. coli* MG1655 was employed for observing red fluorescence. As shown in Figure S8, Supporting Information, the modified bacteria gathered at the periphery of agarose after 60 min. This indicated that PDA had minimal influences on bacterial mobilities. In addition, the photothermal effect of Bac@PDA was tested and the temperature could increase by ≈20 °C after irradiating an 808 nm laser (1 W cm^{-2}) for 5 min (Figure 3G; Figure S9, Supporting Information). Therefore, the photothermal effect of Bac@PDA depended on the concentration of PDA nanoparticles. In a word, the lyophilized PDA nanoparticles maintained a stable connection with *E. coli*. Our combined strategy had a small effect on bacteria activities.

2.4. In Vitro Immunostimulation of BCG@PDA

Apart from the effect of PDA nanoparticles on bacteria activities, the immunostimulation of BCG infected by PDA nanoparticles was also important. First, to explore how the concentration of PDA nanoparticles influenced the immunostimulation of BCG. The activation of RAW264.7 cells was examined following treatment with BCG@PDA. As shown in Figure S10A,B, Supporting Information, the percent of $CD80^+CD86^+$ RAW264.7 cells decreased slightly when the concentration of PDA nanoparticles increased. To evaluate the immune activation of BCG@PDA, we investigated how BCG@PDA regulated macrophages. RAW264.7 cells were incubated with IL-4 for 24 h to acquire M2 macrophages; and then, subjected to different treatments for 24 h to polarize macrophages toward the M1 state. We found that BCG and BCG@PDA could significantly activate macrophages; while, PDA did not affect macrophages (**Figure** 4A). Given that the majority of tumor-associated macrophages are in the M2 state,[18] and inspired by the promising outcomes, we questioned whether BCG@PDA could re-polarize M2 macrophages into the M1 phenotype. First of all, RAW264.7 cells were induced to the M2 state by IL-4 for 24 h; and then, PBS, PDA, BCG, and BCG@PDA were added, followed by incubation for 24 h. The cells were collected and mRNA expression was detected by quantitative real-time polymerase

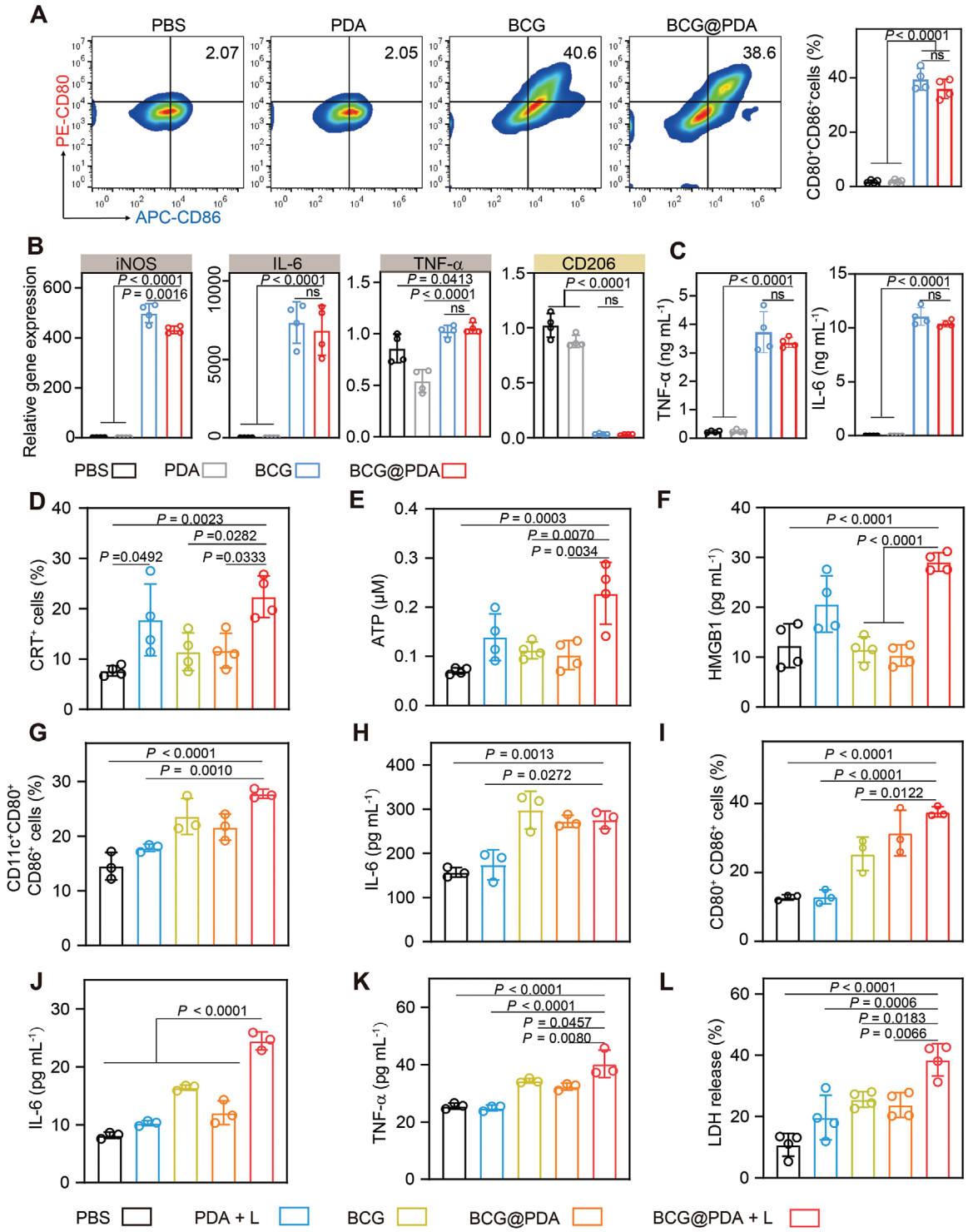

Figure 4. In vitro immune stimulation of BCG@PDA. A) Representative flow cytometric analysis images and relative quantification of $CD80^+CD86^+$ cells in RAW264.7 cells after different treatments ($n = 4$). B) Relative gene expression of iNOS, IL-6, TNF-α, and CD206 in RAW264.7 cells after different treatments ($n = 4$). C) Cytokine levels in the culture medium of RAW 264.7 macrophages after different treatments ($n = 4$). D) Relative quantification of CRT^+ cells in CT26 cells after different treatments ($n = 4$). E) ATP levels in the culture medium of CT26 cells after different treatments ($n = 4$). F) HMGB1 levels in the culture medium of CT26 cells after different treatments ($n = 4$). G) Relative quantification of $CD11c^+CD80^+CD86^+$ cells in BMDCs after different treatments ($n = 3$). H) IL-6 levels in the culture medium of BMDCs after different treatments ($n = 3$). I) Relative quantification of $CD80^+CD86^+$ cells in RAW264.7 cells after different treatments ($n = 3$). J,K) Cytokine levels in the culture medium of RAW 264.7 cells after different treatments ($n = 3$). L) In vitro cytotoxicity of splenocytes toward CT26 cells was measured at an effector/target ratio of 10:1 after being treated for 24 h. Splenocytes were pre-treated with different samples ($n = 4$). Statistical significance was calculated via one-way ANOVA with Bonferroni's post-hoc analysis (A–L).

chain reaction (RT-PCR). As shown in Figure 4B, the mRNA levels of M1 markers (including inducible nitric oxide synthase [iNOS], IL-6, and TNF-α) were significantly increased after being treated by BCG or BCG@PDA. As for CD206, which is the major marker of M2 macrophages, it was downregulated, indicating that macrophages were polarized from the M2 to the M1 phenotype. In addition, an enzyme-linked immunosorbent assay (ELISA) was used to further investigate the polarization of macrophages. Further, the production of TNF-α and IL-6 in the supernatants was much more than in the group treated with PBS (Figure 4C). Further, BCG was employed to study the immunoactivation of DCs. We found BCG could slightly increase the ratio of mature DCs; nevertheless, BCG@PDA had no memorable improvements (Figure S11, Supporting Information). In aggregate, we found that adhering PDA nanoparticles could minimally influence the immunogenicity of BCG, probably because the presence of PDA nanoparticles partly shielded the exposure of bacterial antigens. Therefore, our strategy combined the beneficial qualities of both PDA and BCG.

2.5. In Vitro Synergistically Enhanced Immune Activation

Distinguished from the fact that BCG could activate immune cells directly, PDA-based PTT induced tumor cells ICD with the release of damage-associated molecular patterns (DAMPs).[9b,19] Based on the research above, we believe that BCG@PDA could induce ICD as well when exposed to NIR irradiation. As shown in Figure 4D; Figure S12, Supporting Information, CT26 cells in PDA and BCG@PDA treated groups exposed to the NIR laser exhibited a higher proportion of CRT^+ cells. Moreover, after BCG@PDA with NIR laser treatment, the values of ATP and HMGB-1 in supernatants were significantly increased (Figure 4E,F). Subsequently, the supernatants of the above groups were incubated with bone marrow-derived DCs (BMDCs) for 24 h. The flow cytometric analysis revealed that BMDCs incubated with BCG@PDA with NIR irradiation groups expressed a higher ratio of DC maturation ($CD80^+CD86^+$) (Figure 4G). In the meantime, the T cell activation cytokine (IL-6) secreted by BMDCs was measured by ELISA, which was in line with the flow cytometry results (Figure 4H). Subsequently, we found the supernatants were also able to activate the RAW264.7 cells (Figure 4I; Figure S13A, Supporting Information) and bone marrow-derived macrophages (Figure S13B–D, Supporting Information). The IL-6 and TNF-α levels were upregulated in the culture medium of RAW264.7 cells after being treated by BCG@PDA (Figure 4J,K). In the end, the lactate dehydrogenase (LDH) assay was used to explore the cytotoxicity effect of splenic cells toward CT26 cells. As expected, splenic cells that had been pretreated with the supernatants of group BCG@PDA + L were more susceptible to the tumor cells (Figure 4L). The immunotoxicity of splenic cells was only marginally enhanced by other groups in comparison to the PBS group. These results demonstrate that PTT induces immunogenic death of tumor cells.

BCG as pathogen-associated molecular patterns (PAMPs) can be recognized by immune cells through toll-like receptors (TLRs), thereby activating immune cells through TLR signaling pathways.[20] Studies have elucidated that BCG activates macrophages through the TLR/MyD88 pathway.[11c,15b] A western blotting assay was performed to explore whether BCG-activated macrophages were also associated with these pathways (Figure S14, Supporting Information). A significant increase in the expression levels of TLR2, TLR4, MyD88, and phosphorylated NF-κB was observed in RAW264.7 cells after incubation with the supernatant of group BCG@PDA + L. These results demonstrate that the anti-tumor effect of BCG@PDA was a result of the synergistic combination of PTT and BCG immunotherapy. These PAMPs and DAMPs act as "find me" signals (ATP and HMGB1) or "eat me" signals (BCG@PDA and CRT), which enhance the subsequent immune response.[21]

2.6. In Vivo Antitumor Immune Responses of BCG@PDA

Encouraged by the antitumor responses in vitro, we characterized the efficacy of BCG@PDA in activating the tumor immunosuppressive microenvironment in mouse subcutaneous CT26 tumor models. This was done considering that intratumoral injection has been widely adopted as a therapeutic approach in the field of solid tumor immunotherapy.[22] This method was also utilized in the process of the treatment. When the volume of the tumor reached 100 mm^3, BCG@PDA was intratumorally injected into the tumor site, which subsequently received laser exposure (808 nm, 1 W cm^{-2}) for 3 min. After 5 days, mice were euthanized and the tissues of the CT26 tumor, spleen, and lymph node were collected for analysis (**Figure 5A**). Similarly, PBS, BCG, PDA with laser (PDA + L), and BCG@PDA treatments were carried out as controls. Compared to PBS, BCG, PDA + L, and BCG@PDA groups, the BCG@PDA + L group remarkably improved the percentage of macrophage cells in tumor tissues (Figure S15A, Supporting Information). Therefore, the ratio of M1 macrophages ($CD11b^+CD80^+CD86^+$) improved by 2.2-fold compared to the PBS group (Figure 5B; Figure S15B, Supporting Information). Together with immunofluorescent staining of CD206 (Figure 5I), we concluded that the BCG@PDA group could increase the M1 type macrophages and diminish the M2 type macrophages, which could explicate the immune effect of BCG@PDA in vivo. In addition, the ratio of mature DCs ($CD11c^+CD80^+CD86^+$) in the BCG@PDA + L group was significantly increased in the tumor sites (Figure 5C; Figure S16A,B, Supporting Information). Meanwhile, the inguinal lymph nodes closed to tumor sites were also collected and analyzed. The proportion of mature DCs in the BCG@PDA + L group was also improved compared to the PBS group (Figure 5D; Figure S16C,D, Supporting Information). T lymphocytes are powerful weapons against tumors. Both M1 macrophages and DCs could recognize the tumor antigens induced by PTT and present them to T cells.[23] The infiltrating T lymphocytes in tumor tissues were further investigated. As shown in Figure 5E; Figure S17A,B, Supporting Information, the ratio of cytotoxic T lymphocytes (CTLs) ($CD3^+CD8^+$) in the BCG@PDA + L group showed a significant increase compared with the PBS group. Meanwhile, an increase of T cells ($CD3^+$) had also been observed in the spleen, the major immune organ (Figure S17C, Supporting Information). The CTLs in the spleen were upregulated as well (Figure 5F; Figure S17D, Supporting Information). Finally, the concentrations of IL-6 and TNF-α in the serum of CT26-bearing mice showed an increase upon receiving the combination therapy

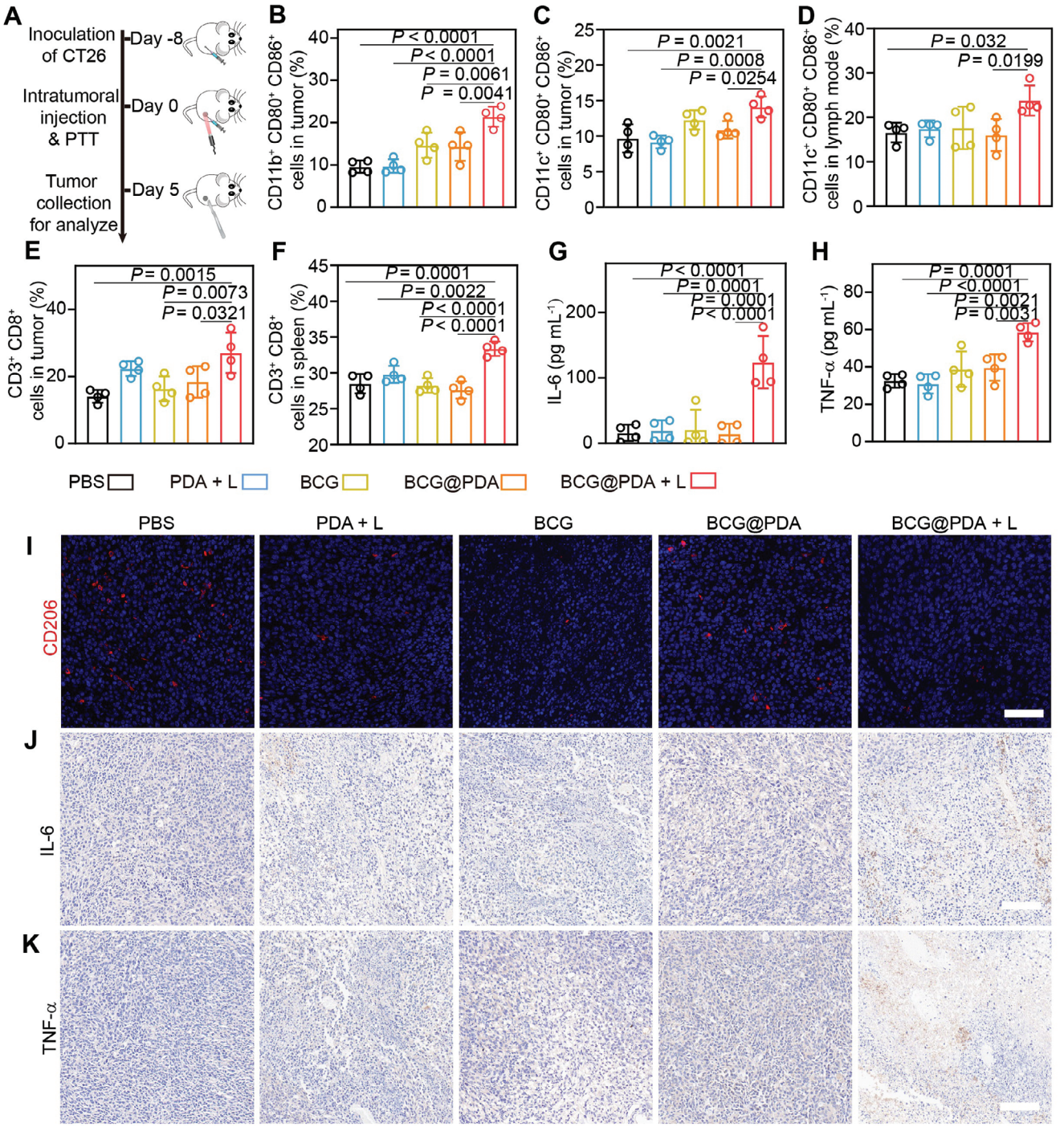

Figure 5. In vivo immune stimulation of BCG@PDA. A) Schematic representation of immunoassay. B) Relative quantification of M1 macrophages ($CD11b^+CD80^+CD86^+$) in tumors following different treatments ($n = 4$). C) Relative quantification of DCs ($CD11c^+CD80^+CD86^+$) in tumors following different treatments ($n = 4$). D) Relative quantification of DCs ($CD11c^+CD80^+CD86^+$) in lymph nodes following different treatments ($n = 4$). E) Relative quantification of $CD3^+CD8^+$ T cells in tumor tissues with different treatments ($n = 4$). F) Relative quantification of $CD3^+CD8^+$ T cells in spleen with different treatments ($n = 4$). G,H) Serum cytokine content, including IL-6 (G) and TNF-α (H), after diverse treatments ($n = 4$). I) Representative immunofluorescence images of M2 macrophages (red: CD206, blue: DAPI) in tumor tissues of different groups (scale bar: 100 µm). J,K) Immunohistochemistry staining of IL-6 and TNF-α of tumor sections. Scale bar: 100 µm. Statistical significance was calculated via one-way ANOVA with Bonferroni's post-hoc analysis (B–H).

(Figure 5G,H). Similarly, the results of immunohistochemical staining of IL-6 and TNF-α were in agreement with the results of ELISA (Figure 5J,K). Taken together, these findings demonstrated that the combination of BCG@PDA with PTT triggered a robust innate immune response in tumor sites.

2.7. In Vivo Therapeutic Efficacy of Combined Photothermal and Immunotherapy

Encouraged by the potent immune response induced by BCG@PDA, we evaluated the therapeutic potential of our strategy by employing subcutaneous CT26 tumor-bearing mice. Similarly, CT26-bearing mice were divided into five groups: PBS, PDA + L, BCG, BCG@PDA, and BCG@PDA + L, respectively. Tumor volume, body weight, and animal survival were monitored to evaluate the therapeutic effect (**Figure 6**A). As described in Figure 6B,C, among all treatment groups, the single intratumoral BCG@PDA injection combined with NIR irradiation led to the smallest average tumor size. In addition, the body weight of mice did not change obviously throughout the various treatments (Figure 6D). BCG@PDA with laser treatment significantly slowed tumor growth, 71% of the animals survived for 50 days, whereas mice in other groups failed to survive for more than 38 days (Figure 6E). From hematoxylin and eosin (H&E) staining and terminal deoxynucleotidyl transferase-mediated dUTP nick-end labeling (TUNEL), the tumor cell apoptosis after the treatment by BCG@PDA with laser was further confirmed (Figure 6F). The groups treated with PBS and BCG@PDA had normal morphology and no apoptotic tumor cells, whereas those treated with BCG and PDA + L had a small number of apoptotic tumor cells. Notably, the mice treated with BCG@PDA + L had the greatest number of damaged cancer cells. Moreover, an inconspicuous cell proliferation signal (Ki67) was found in mice treated with BCG@PDA with laser, indicating that BCG@PDA had a significant inhibitory effect on tumors when exposed to NIR light (Figure 6F).

The therapeutic effect of BCG@PDA was also evaluated in the orthotopic implantation colorectal model. First, an orthotopic implantation colorectal mice model was established and received different treatments (**Figure 7**A). CT26-luc cells were injected into the caecum of mice. Five days later, the mice received treatment. During the treatment process, mice were anesthetized with isoflurane and the treatment was monitored in real-time using an infrared camera (Figure 7B).[24] The progression of tumors in mice was observed through the bioluminescence of CT26-luc cells (Figure 7C). Compared with other groups, the BCG@PDA + L group displayed a smaller tumor volume, characterized by the weakest bioluminescence. Through the quantitative examination of bioluminescence intensity in CT26-luc bearing mice with orthotopic tumors, the BCG@PDA + L group showed significant tumor inhibitory effects compared with controls (Figure 7D). The BCG and PDA + L groups also exhibited a slight inhibition effect of tumor growth and that was consistent with the expected. Moreover, based on the visual evidence provided by the photographs and the size of the tumors, it can be concluded that the BCG@PDA + L group exhibited the most favorable outcome in terms of treatment efficacy (Figure 7E; Figure S18, Supporting Information). The results from the histopathological examination showed that there were no apparent signs of tumor tissue present in the colon of the BCG@PDA + L group, aligning with our previous research outcomes (Figure 7F). In conclusion, these outcomes recommended that BCG@PDA joining with NIR could significantly kill cancer cells as a potential therapy for malignant tumor treatment.

2.8. Biocompatibility of BCG@PDA

To determine the in vivo toxicity of BCG@PDA, the mice were sacrificed after in vivo anticancer treatment, and the major organs (heart, liver, spleen, lung, and kidney) were collected for H&E staining. Histological analysis showed that there were no significant pathological changes in the organs after various treatments (Figure S19, Supporting Information). This suggests that the BCG@PDA had little effect on the CT26 tumor-bearing mice during the treatment. In addition, the blood samples of mice were collected for investigating the in vivo biosecurity. The outcomes of liver and kidney functions remained within the acceptable range (Figure S20A–D, Supporting Information). The blood routine results of all groups did not exhibit any significant systemic toxicity (Figure S20E, Supporting Information). These findings demonstrated that BCG@PDA was biocompatible for biomedical applications without detectable side effects.

3. Conclusion

In conclusion, our study highlights the potential of combining lyophilized PDA nanoparticles with BCG for photothermal immunotherapy. The use of this approach results in a powerful synergy, offering two distinct benefits, that is, the direct elimination of tumor cells and the stimulation of an immune response against any remaining cancerous cells. Specifically, when BCG@PDA is injected into the tumor site and exposed to light, it effectively kills cancer cells. The presence of light triggers a photothermal effect in PDA nanoparticles, leading to ICD of tumor cells and stimulating the release of HMGB1 and ATP, and enhancing the expression of CRT. These responses further activate DCs and macrophages to release pro-inflammatory cytokines. Meanwhile, after being modified with PDA nanoparticles, BCG still retains its potent immunostimulatory effect. Upon activation, immune cells transport fragments of the defeated tumor to lymphoid tissues, where they present the derived antigens to T cells. Equipped with this specific recognition, T cells systematically patrol the body, identifying and eliminating any remaining malignant cells with precise accuracy. This cascading process results in a strong innate immune response at the primary location of the tumor, laying the foundation for the development of a comprehensive, systemic anticancer immunity.

Extending beyond the immediate benefits, our research has also explored the logistical aspect of therapeutic delivery. Our findings show that PDA nanoparticles can withstand storage at freezing temperatures, maintaining their structural and functional integrity at −20 °C. Practically speaking, PDA nanoparticles retain their characteristic particle size and preserve their capacity for photothermal conversion. The long-term stability in storage creates opportunities for their integration into clinical settings, providing a convenient and shelf-stable solution for clinical translation.

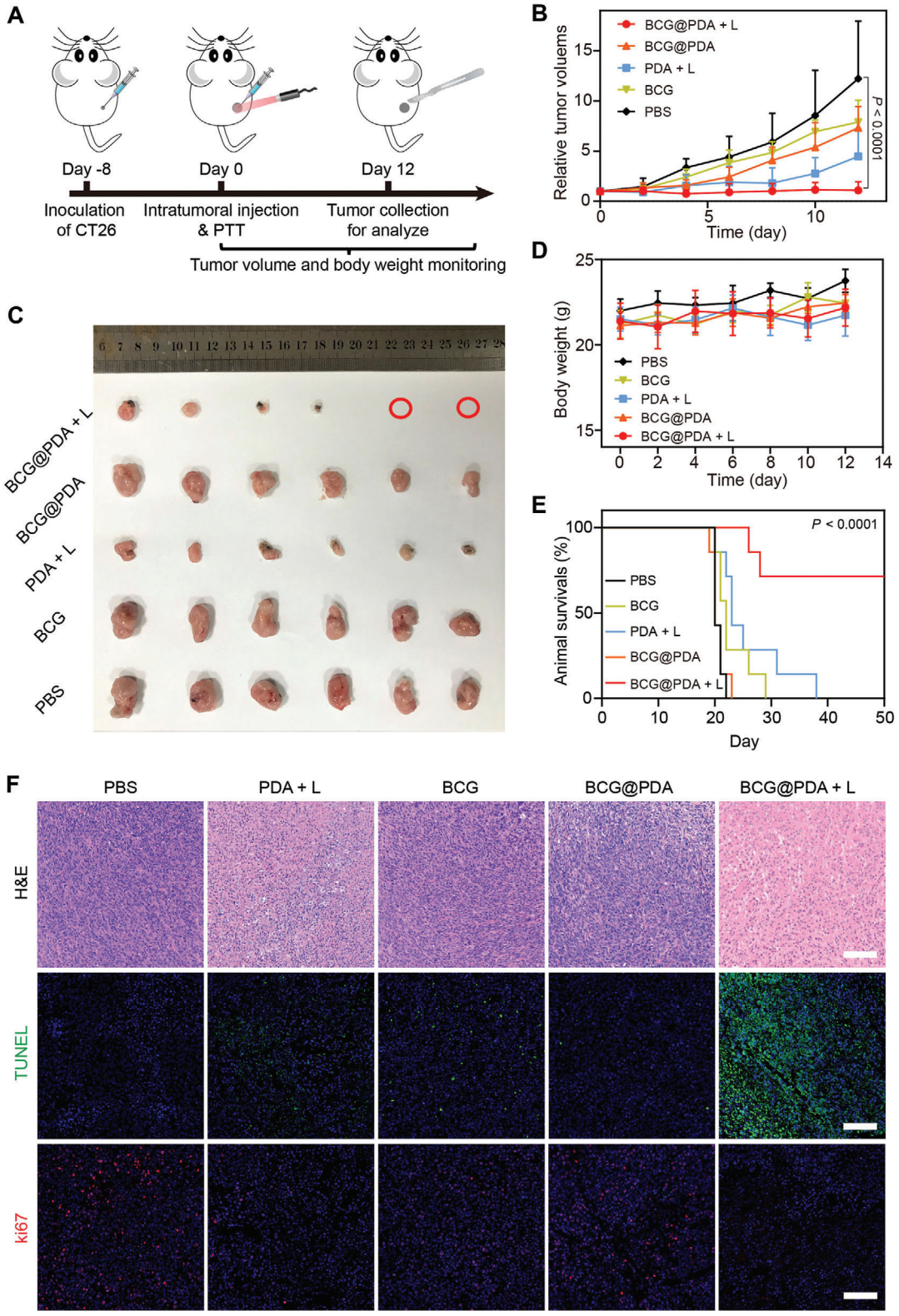

Figure 6. Anti-tumor effect of BCG@PDA in the subcutaneous tumor. A) Schematic representation of subcutaneous CT26 tumor antitumor therapy. B) Tumor growth curves after different treatments ($n = 6$). C) Image of tumors captured on Day 12, showing tumor-bearing mice treated with various therapies ($n = 6$). D) Changes in body weight of different groups ($n = 6$). E) Survival rates of CT26 tumor-bearing mice in different groups ($n = 7$). F) H&E, TUNEL, and immunofluorescence staining of Ki67 of tumor tissues after various treatments for 12 days. Scale bar: 100 µm. Statistical significance was calculated via one-way ANOVA with Bonferroni's post-hoc analysis (B,E).

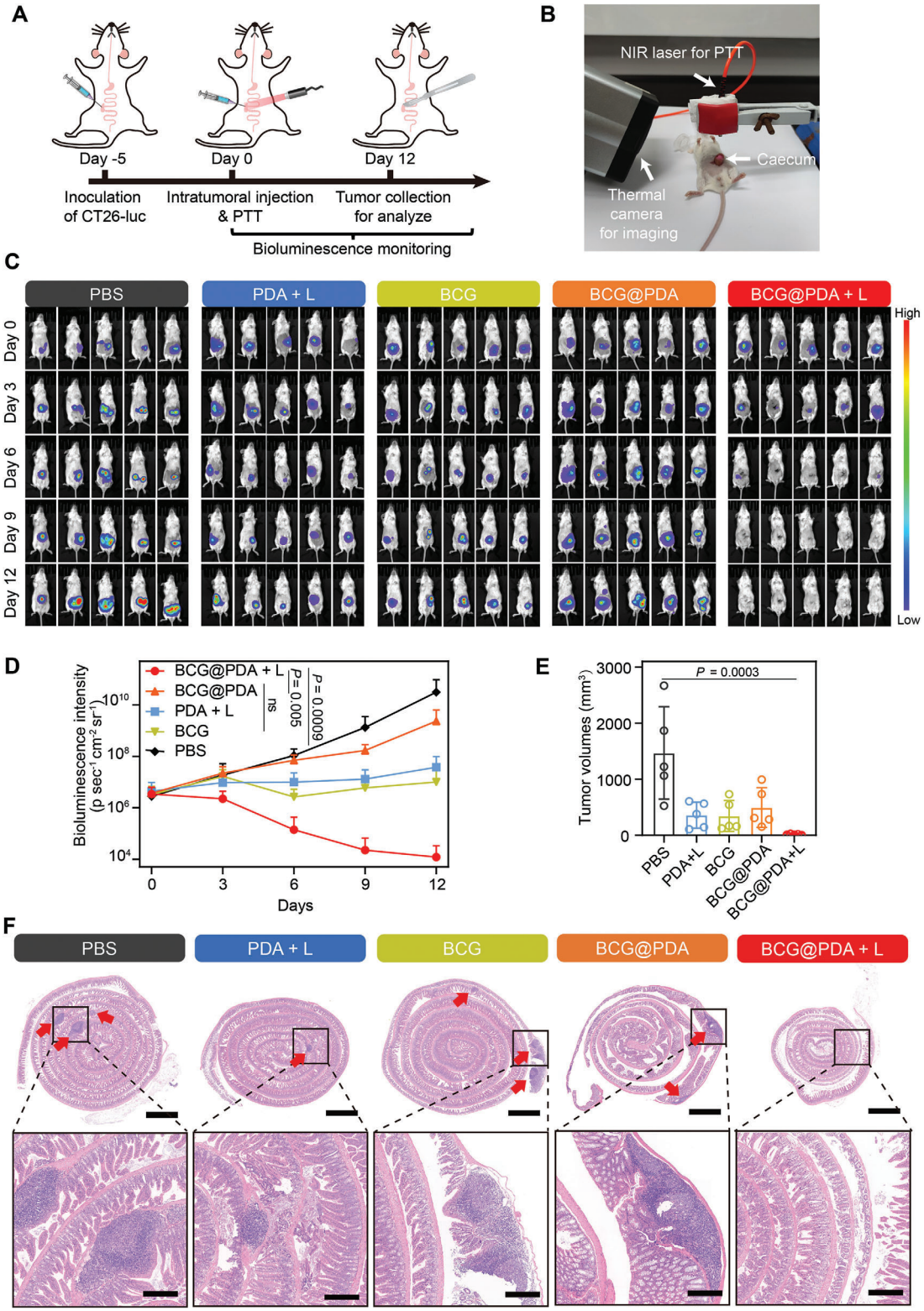

Figure 7. Anti-tumor effect of BCG@PDA in the orthotopic colorectal cancer. A) Schematic representation of orthotopic CT26-luc tumor antitumor therapy. B) Photograph of PTT process in mice. C) In vivo bioluminescence imaging of orthotopic CT26-luc tumor-bearing mice after receiving different treatments ($n = 5$). D) In vivo bioluminescence quantitative analysis of orthotopic CT26-luc tumor-bearing mice after receiving different treatments ($n = 5$). E) Tumor volumes of CT26-luc tumor-bearing mice after receiving different treatments at day 12 ($n = 5$). F) H&E staining of colon tissues after various treatments for 12 days. Red arrows mark the location of the tumors (scale bar: 500 μm). Below is an enlarged view of a selected area (scale bar: 100 μm). Statistical significance was calculated via the Kruskal–Wallis test (D,E).

4. Experimental Section

Methods and any associated references are available in the Supporting Information.

Supporting Information

Supporting Information is available from the Wiley Online Library or from the author.

Acknowledgements

Z.-N.Z. and Y.-D.Q. contributed equally to this work. This work was supported by the National Natural Science Foundation of China (51988102, 52273148, 52333004, and 22135005). The authors thank the Core Facility of Wuhan University for assisting with the SEM measurement and ICP-MS analysis. All animal experiments were approved by the Institutional Animal Care and Use Committee (IACUC) of the Animal Experiment Center of Wuhan University (Wuhan, China).

Conflict of Interest

The authors declare no conflict of interest.

Data Availability Statement

The data that support the findings of this study are available from the corresponding author upon reasonable request.

Keywords

Bacillus Calmette–Guérin, colorectal cancer, immunotherapy, photothermal therapy, polydopamine

Received: March 12, 2024
Revised: July 15, 2024
Published online:

[1] H. Sung, J. Ferlay, R. L. Siegel, M. Laversanne, I. Soerjomataram, A. Jemal, F. Bray, *CA: Cancer J. Clin.* **2021**, *71*, 209.
[2] W. B. Strum, *N. Engl. J. Med.* **2016**, *374*, 1065.
[3] a) Y. Liu, K. Ai, J. Liu, M. Deng, Y. He, L. Lu, *Adv. Mater.* **2013**, *25*, 1353; b) W. Chen, Y. Wang, M. Qin, X. Zhang, Z. Zhang, X. Sun, Z. Gu, *ACS Nano* **2018**, *12*, 5995.
[4] Q. Cheng, F. Gao, W. Y. Yu, M. Z. Zou, X. L. Ding, M. J. Li, S.-X. Cheng, X.-Z. Zhang, *Adv. Funct. Mater.* **2020**, *30*, 2000335.
[5] L. Zhou, B. Feng, H. Wang, D. Wang, Y. Li, *Nano Today* **2022**, *44*, 101466.
[6] K. Hu, L. Xie, Y. Zhang, M. Hanyu, Z. Yang, K. Nagatsu, H. Suzuki, J. Ouyang, X. Ji, J. Wei, *Nat. Commun.* **2020**, *11*, 2778.
[7] X. Li, J. F. Lovell, J. Yoon, X. Chen, *Nat. Rev. Clin. Oncol.* **2020**, *17*, 657.
[8] G. Shafirstein, D. Bellnier, E. Oakley, S. Hamilton, M. Potasek, K. Beeson, E. J. C. Parilov, *Cancers* **2017**, *9*, 12.
[9] a) R.-H. Deng, M.-Z. Zou, D. Zheng, S.-Y. Peng, W. Liu, X.-F. Bai, H.-S. Chen, Y. Sun, P.-H. Zhou, X.-Z. Zhang, *ACS Nano* **2019**, *13*, 8618; b) W. Chen, Z. Guo, Y. Zhu, N. Qiao, Z. Zhang, X. Sun, *Adv. Funct. Mater.* **2020**, *30*, 1906623; c) J. Li, Q. Xia, H. Guo, Z. Fu, Y. Liu, S. Lin, J. Liu, *Angew. Chem., Int. Ed.* **2022**, *134*, 202202409.
[10] X. Li, T. Yong, Z. Wei, N. Bie, X. Zhang, G. Zhan, J. Li, J. Qin, J. Yu, B. Zhang, *Nat. Commun.* **2022**, *13*, 2794.
[11] a) S. Zhou, C. Gravekamp, D. Bermudes, K. Liu, *Nat. Rev. Cancer* **2018**, *18*, 727. b) C. Wang, L. Chen, J. Zhu, C. Wang, M. Li, Y. Miao, N. Liu, Z. Ji, F. Pan, Y. Liu, J. Zhu, Y. Yang, Q. Chen, *Adv. Funct. Mater.* **2024**, *34*, 2316092; c) K. Liu, L. Wang, J. Peng, Y. Lyu, Y. Li, D. Duan, W. Zhang, G. Wei, T. Li, Y. Niu, Y. Zhao, *Adv. Mater.* **2024**, *36*, 2310735; d) C. R. Gurbatri, N. Arpaia, T. Danino, *Science* **2022**, *378*, 858.
[12] M. Li, J. Wu, N. Li, J. Zhou, W. Cheng, A. Wu, L. Liu, N. Jiao, *Adv. Funct. Mater.* **2024**, 2402333.
[13] a) L. Lei, J. Yan, K. Xin, L. Li, Q. Sun, Y. Wang, T. Chen, S. Wu, J. Shao, B. Liu, X. Chen, *ACS Nano* **2024**, *18*, 12194. b) Y. Chen, X. Chen, W. Bao, G. Liu, W. Wei, Y. Ping, *Nat. Biotechnol.* **2024**, https://doi.org/10.1038/s41587-023-02118-7.
[14] a) C. Pettenati, M. A. Ingersoll, *Nat. Rev. Urol.* **2018**, *15*, 615; b) G. Redelman-Sidi, M. S. Glickman, B. H. Bochner, *Nat. Rev. Urol.* **2014**, *11*, 153.
[15] a) R. J. Arts, A. Carvalho, C. L. Rocca, C. Palma, F. Rodrigues, R. Silvestre, J. Kleinnijenhuis, E. Lachmandas, L. G. Gonçalves, A. Belinha, *Cell Rep.* **2016**, *17*, 2562; b) J. H. van Puffelen, S. T. Keating, E. Oosterwijk, A. G. van der Heijden, M. G. Netea, L. A. B. Joosten, S. H. Vermeulen, *Nat. Rev. Urol.* **2020**, *17*, 513.
[16] a) J. B. Vermorken, A. M. Claessen, H. Van Tinteren, H. E. Gall, R. Ezinga, S. Meijer, R. J. Scheper, C. J. Meijer, E. Bloemena, J. H. Ransom, *Lancet* **1999**, *353*, 345; b) C. Uyl-de Groot, J. Vermorken, M. Hanna Jr., P. Verboom, M. Groot, G. Bonsel, C. Meijer, H. Pinedo, *Vaccine* **2005**, *23*, 2379.
[17] P. Fonte, S. Reis, B. Sarmento, *J. Controlled Release* **2016**, *225*, 75.
[18] a) R. H. Deng, M. Z. Zou, D. Zheng, S. Y. Peng, W. Liu, X. F. Bai, H. S. Chen, Y. Sun, P. H. Zhou, X. Z. Zhang, *ACS Nano* **2019**, *13*, 8618; b) N.-B. Hao, M.-H. Lu, Y.-H. Fan, Y.-L. Cao, Z.-R. Zhang, S.-M. Yang, *J. Immunol. Res.* **2012**, *2012*, 948098; c) Y. Pan, Y. Yu, X. Wang, T. Zhang, *Front. Immunol.* **2020**, *11*, 583084.
[19] J. Li, Q. Xia, H. Guo, Z. Fu, Y. Liu, S. Lin, J. J. A. C. Liu, *Angew. Chem., Int. Ed.* **2022**, *134*, 202202409.
[20] M. Foster, P. C. Hill, T. P. Setiabudiawan, V. A. C. M. Koeken, B. Alisjahbana, R. van Crevel, *Immunol. Rev.* **2021**, *301*, 122.
[21] Z. Yang, D. Gao, J. Zhao, G. Yang, M. Guo, Y. Wang, X. Ren, J. S. Kim, L. Jin, Z. Tian, X. Zhang, *Nat. Rev. Clin. Oncol.* **2023**, *20*, 116.
[22] I. Melero, E. Castanon, M. Alvarez, S. Champiat, A. Marabelle, *Nat. Rev. Clin. Oncol.* **2021**, *18*, 558.
[23] a) Y. Lv, F. Li, S. Wang, G. Lu, W. Bao, Y. Wang, Z. Tian, W. Wei, G. J. S. A. Ma, *Sci. Adv.* **2021**, *7*, eabd7614; b) K. Liu, Y. Liao, Z. Zhou, L. Zhang, Y. Jiang, H. Lu, T. Xu, D. Yang, Q. Gao, Z. Li, S. Tan, W. Cao, F. Chen, G. Li, *Biomaterials* **2022**, *282*, 121383.
[24] S. Gao, G. Wei, S. Zhang, B. Zheng, J. Xu, G. Chen, M. Li, S. Song, W. Fu, Z. Xiao, W. Lu, *Nat. Commun.* **2019**, *10*, 2206.